A STOCHASTIC FRAMEWORK FOR ATOMISTIC FRACTURE[*]

MACIEJ BUZE[†], THOMS E. WOOLLEY[†], AND ANGELA MIHAI[†]

Abstract. We present a stochastic modeling framework for atomistic propagation of a Mode I surface crack, with atoms interacting according to the Lennard–Jones interatomic potential at zero temperature. Specifically, we invoke the Cauchy–Born rule and the maximum entropy principle to infer probability distributions for the parameters of the interatomic potential. We then study how uncertainties in the parameters propagate to the quantities of interest relevant to crack propagation, namely, the critical stress intensity factor and the lattice trapping range. For our numerical investigation, we rely on an automated version of the so-called numerical-continuation enhanced flexible boundary NCFlex algorithm.

1. Introduction. Brittle fracture in crystalline materials is an inherently multiscale phenomenon where macroscopic crack propagation is determined by atomistic processes occurring at the crack tip [1]. The usual modeling approach consists in coupling a high-level, high-accuracy atomistic model, employed in the vicinity of the crack tip, with a continuum-modeled far field. The atomistic model should ideally exhibit a quantum level of accuracy, which can be achieved, for instance, with a density functional theory type model [17]. A more computationally feasible alternative is to disregard the electrons and model the interatomic interactions instead. In this framework, atoms are treated as points in a discrete model and the behavior of atoms is governed by an empirical (but physics-based) interatomic potential. At this level of description, the two quantities that capture the propagation of a straight crack of single mode are the *critical stress intensity factor* K_c and, reflecting the discreteness of the lattice, the *lattice trapping range*, $(K_-, K_+) \subset \mathbb{R}$, which was first identified in [31].

A typical empirical potential has between 2 and 11 parameters (rising to > 1000 for modern machine-learning potentials), and the highly nonlinear nature of the overall model necessitates quantifying the uncertainty in their choice and how this propagates to quantities of interest. Usually, this is achieved by employing a Bayesian approach, whereby one assumes some prior probability distributions for the parameters, which are subsequently updated using available data originating from experiments or higher-level theories [10, 21, 34]. However, two main issues can arise with this approach. First, the prior distribution of each parameter is typically taken to be a Gaussian (e.g., in [10, 21, 34]), due to the seemingly reasonable assumption that errors in the reference data set are independent. This may not always be correct, depending on the physical constraints present in the model, such as, for example, when

[†]School of Mathematics, Cardiff University, Cardiff, CF24 4AG (buzem@cardiff.ac.uk, WoolleyT1@cardiff.ac.uk, MihaiLA@cardiff.ac.uk).

parameters must have positive values. Second, while the Bayesian procedure can be carried out reasonably well for simple quantities of interest, including elastic moduli, lattice parameters, cohesion energy, and point-defect formation energy, it presents a computational challenge for more complicated quantities, such as (K_-, K_+), for which analytical formulae do not exist and can only be estimated numerically.

Addressing the first issue and inspired by the recent literature on the topic of continuum stochastic elasticity [28, 13, 29, 14, 12, 24], we propose an information-theoretic approach to derive prior distributions for the parameters of the interatomic potential. Our approach uses a minimal set of physical constraints obtained by coupling the atomistic model via the Cauchy–Born rule with its continuum counterpart. Regarding the computational challenge, we formalize an automated numerical procedure that allows a reasonably fast computation of K_c and (K_-, K_+). This is based on a recently proposed NCFlex (numerical continuation-enhanced flexible boundary) scheme [5].

We demonstrate our approach for an idealized model of straight Mode I fracture in a two-dimensional (2D) crystalline material forming a triangular lattice. In particular, we focus on the Lennard–Jones potential [20], which has two parameters, one representing the energetic cost of breaking a bond and the other specifying how difficult it is to break a bond. The relative simplicity of the model ensures that the stochastic framework can be presented with clarity and allows us to compare our numerical results with some analytical results available in this case. In particular, we show that, in our model, the relative strength of lattice trapping is small and does not depend on the choice of parameters. We further provide evidence that the continuum-theory based formula for K_c does hold for our model. We also highlight the interplay between the strength of statistical fluctuations and lattice trapping. In section 2, we discuss our prerequisites, summarizing the classical continuum framework of linearized elasticity (CLE), and outline the information-theoretic approach, together with a brief account of how this framework translates to fracture modeling. In section 3, we present the deterministic atomistic model, which uses CLE as a far-field boundary condition. Section 4 is devoted to the development of our atomistic stochastic framework and is followed by the numerical investigation in section 5. Some detailed calculations are deferred to Appendix A.

2. Prerequisites.

2.1. Classical linearized elasticity. We consider elastic deformations, $\boldsymbol{y} : \Omega \to \mathbb{R}^3$, of a 3D body, $\Omega \subset \mathbb{R}^3$, of the form $\boldsymbol{y}(\boldsymbol{x}) = \boldsymbol{x} + \boldsymbol{u}(\boldsymbol{x})$, where $\boldsymbol{u} : \Omega \to \mathbb{R}^3$ is the displacement field. The *linearized strain tensor*, $\boldsymbol{\varepsilon} : \Omega \to \mathbb{R}^{3 \times 3}$, is defined by $\boldsymbol{\varepsilon}(\boldsymbol{x}) = \left[\nabla \boldsymbol{u}(\boldsymbol{x}) + \nabla \boldsymbol{u}(\boldsymbol{x})^\top \right] / 2$, and the linear elastic constitutive stress-strain relation [19] takes the form

$$(2.1) \qquad\qquad \boldsymbol{\sigma}(\boldsymbol{x}) = \mathbb{C} : \boldsymbol{\varepsilon}(\boldsymbol{x}),$$

where $\mathbb{C} \in \mathbb{R}^{3 \times 3 \times 3 \times 3}$ is a constant fourth-order tensor, known as the *elasticity tensor*, and $\boldsymbol{\sigma} : \Omega \to \mathbb{R}^{3 \times 3}$ is the *stress tensor*. In the absence of body forces, equilibrium configurations can be found by solving the equations

$$(2.2) \qquad\qquad \sigma_{ij,j} = 0 \ \text{ for } i = 1, 2, 3,$$

where Einstein summation convention is used, subject to appropriate boundary conditions. Depending on the symmetry class considered, the elasticity tensor $\mathbb{C}$ has up to 21 independent entries [19], known as *elasticities*, and admits a second-order tensor

representation [22], in the form of a symmetric matrix $[\mathbb{C}] \in \mathbb{R}^{6 \times 6}$. Then the relation (2.1) can be equivalently restated as follows:

$$
(2.3) \quad
\begin{bmatrix}
\sigma_{11} \\
\sigma_{22} \\
\sigma_{33} \\
\sigma_{23} \\
\sigma_{31} \\
\sigma_{12}
\end{bmatrix}
=
\begin{bmatrix}
\mathbb{C}_{1111} & \mathbb{C}_{1122} & \mathbb{C}_{1133} & \mathbb{C}_{1123} & \mathbb{C}_{1131} & \mathbb{C}_{1112} \\
\mathbb{C}_{2211} & \mathbb{C}_{2222} & \mathbb{C}_{2233} & \mathbb{C}_{2223} & \mathbb{C}_{2231} & \mathbb{C}_{2212} \\
\mathbb{C}_{3311} & \mathbb{C}_{3322} & \mathbb{C}_{3333} & \mathbb{C}_{3323} & \mathbb{C}_{3331} & \mathbb{C}_{3312} \\
\mathbb{C}_{2311} & \mathbb{C}_{2322} & \mathbb{C}_{2333} & \mathbb{C}_{2323} & \mathbb{C}_{2331} & \mathbb{C}_{2312} \\
\mathbb{C}_{3111} & \mathbb{C}_{3122} & \mathbb{C}_{3133} & \mathbb{C}_{3123} & \mathbb{C}_{3131} & \mathbb{C}_{3112} \\
\mathbb{C}_{1211} & \mathbb{C}_{1222} & \mathbb{C}_{1233} & \mathbb{C}_{1223} & \mathbb{C}_{1231} & \mathbb{C}_{1212}
\end{bmatrix}
\begin{bmatrix}
\varepsilon_{11} \\
\varepsilon_{22} \\
\varepsilon_{33} \\
2\varepsilon_{23} \\
2\varepsilon_{31} \\
2\varepsilon_{12}
\end{bmatrix}.
$$

In every symmetry class, $[\mathbb{C}]$ can be decomposed as follows:

$$
(2.4) \qquad\qquad [\mathbb{C}] = \sum_{i=1}^{n} c_i \boldsymbol{E_i},
$$

where n ranges from 2 for the fully isotropic case to 21 when a fully anisotropic case is considered. Here, $\{\boldsymbol{E_i}\}$ is the corresponding basis of a subspace of $\mathbb{R}^{6 \times 6}$ (see, e.g., [13]) and

$$
(2.5) \qquad\qquad \boldsymbol{c} = (c_1, \ldots, c_n) \in \mathbb{R}^n
$$

is the set of independent entries of $\mathbb{C}$.

2.2. An information-theoretic approach for continuum elastic materials. To account for the inherent uncertainty in elastic material parameters, the elasticity tensor can be modeled as a random variable. At the continuum level, the randomness typically stems from (i) the presence of uncertainties while modeling the experimental setup in either forward simulations or inverse identification and (ii) the lack of scale separation for heterogeneous random materials, resulting in the consideration of mesoscopic apparent properties. In [13], a least-informative stochastic modeling framework for elastic material is developed by invoking the maximum entropy principle (MaxEnt) [16]. The minimal set of constraints to explicitly construct a MaxEnt prior probability distribution for $\mathbb{C}$ is as follows:
- (P1) The mean value of the tensor is known.
- (P2) The elasticity tensor $\mathbb{C}$, and its inverse, known as the *compliance tensor*, have a finite second-order moment (physical consistency).

A more detailed treatment of this class of approaches can be found in [28, 29, 14, 12]. Given the decomposition of $[\mathbb{C}]$ in (2.4), the object of interest is an $\mathbb{R}^n$-valued random variable $\boldsymbol{c}$, and the constraints (P1)–(P2) (together with the required normalization) take the form of a mathematical expectation

$$
(2.6) \qquad\qquad \mathbb{E}\{\boldsymbol{f}(\boldsymbol{c})\} = \boldsymbol{h},
$$

where $\boldsymbol{f} : \mathbb{R}^n \to \mathbb{R}^q$ and $\boldsymbol{h} \in \mathbb{R}^q$. It can be shown [16, 23] that the MaxEnt probability distribution of the random variable $\boldsymbol{c}$ from (2.5) is characterized by the probability density function

$$
(2.7) \qquad\qquad \rho(\mathfrak{c}) := \mathbf{1}_S(\mathfrak{c}) \exp\{-\langle \boldsymbol{\lambda}, \, \boldsymbol{f}(\mathfrak{c}) \rangle_{\mathbb{R}^q}\},
$$

where the set $S \subset \mathbb{R}^n$ represents all possible choices of $\boldsymbol{c} \in \mathbb{R}^n$ for which (2.6) is satisfied, whereas $\boldsymbol{\lambda} = (\lambda_1, \ldots, \lambda_q)$ is the vector of the associated Lagrange multipliers. We refer to [13] for an in-depth discussion, and in particular, to their Appendix B, in which the existence and uniqueness of a MaxEnt probability density function is addressed, explaining why this takes the form (2.7).
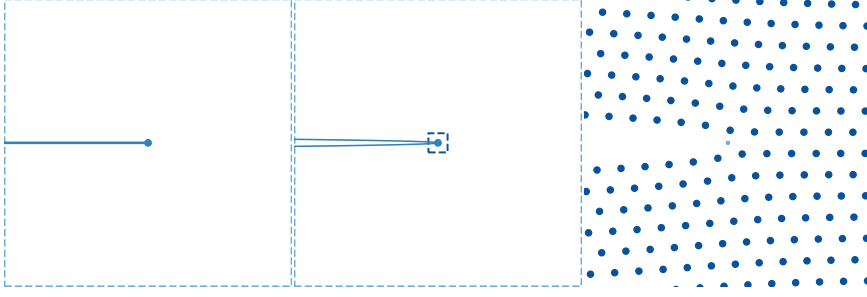
FIG. 1. *Left: A continuum $\mathbb{R}^2 \setminus \Gamma_0$ in the reference configuration. Middle: The configuration of a cracked body obtained from the equilibrium displacement field $\boldsymbol{u}$ from (2.9), with the vicinity of the crack tip (in which atomistic effects dominate) highlighted. Right: The atomistic structure in the vicinity of the crack tip.*

2.3. Mode I fracture in planar elasticity. Our stochastic framework for atomistic crack propagation will be presented for the case of a single Mode I crack in a cubic crystal modeled in the in-plane approximation (see Figure 1). This leads to considerable simplification of the general theory presented in section 2.1.

In *planar elasticity* [32] (see [26, Appendix] for a discussion on the plane-strain and plane-stress reductions of the 3D elasticity theory), the strain components are $\varepsilon_{11}, \varepsilon_{22}, \varepsilon_{12}$ and the stress components are $\sigma_{11}, \sigma_{22}, \sigma_{12}$. In combination with the fact that, in the cubic symmetry class, $[\mathbb{C}]$ has three independent entries $\boldsymbol{c} = (c_1, c_2, c_3)$, (2.3) simplifies to

$$\boldsymbol{\sigma}_{2\mathrm{D}} = \mathbb{C}_{2\mathrm{D}} : \boldsymbol{\varepsilon} \iff \begin{bmatrix} \sigma_{11} \\ \sigma_{22} \\ \sigma_{12} \end{bmatrix} = \begin{bmatrix} c_1 & c_2 & 0 \\ c_2 & c_1 & 0 \\ 0 & 0 & c_3 \end{bmatrix} \begin{bmatrix} \varepsilon_{11} \\ \varepsilon_{22} \\ 2\varepsilon_{12} \end{bmatrix}.$$

As will become apparent when we introduce the atomistic setup in section 3, we consider in fact a special case, such that

$$(2.8) \qquad c_2 = c_3 \quad \text{and} \quad c_3 = \frac{c_1 - c_2}{2} \implies c_2 = \frac{1}{3}c_1 = \mu,$$

where μ denotes the *shear modulus* and represents the only independent entry of the elasticity tensor. In this case, an equilibrium displacement field, $\boldsymbol{u} : \mathbb{R}^2 \setminus \Gamma_0 \to \mathbb{R}^2$, around a Mode I crack, with the crack surface described by

$$\Gamma_0 = \{\boldsymbol{x} = (x_1, x_2) \in \mathbb{R}^2 \mid x_1 < 0 \text{ and } x_2 = 0\},$$

and which satisfies the equilibrium equations (2.2) subject to homogeneous Neumann boundary condition on Γ_0, can be shown [30] to be given by

$$(2.9) \qquad K\widehat{\boldsymbol{u}}(\boldsymbol{m}) = \frac{K}{4\sqrt{2\pi}\mu} \sqrt{r} \begin{bmatrix} 3\cos(\theta/2) - \cos(3\theta/2) \\ 5\sin(\theta/2) - \sin(3\theta/2) \end{bmatrix}, \qquad \theta \in (-\pi, \pi),$$

where we employ polar coordinates $\boldsymbol{m} = r(\cos\theta, \sin\theta)$ and $K \in \mathbb{R}$ is the *stress intensity factor* and enters as a prefactor. According to *Griffith's criterion* [30], at the continuum level of description, there exists a critical K_c, so that, when $K > K_\mathrm{c}$,

it is energetically favorable for the crack to propagate. It can be shown [36] that, in the case considered, the critical value is

$$(2.10) \qquad \widetilde{K}_{\text{cont}} = 4\sqrt{\frac{\gamma\mu}{3}},$$

where γ is the surface energy per unit area, which is a material-dependent quantity.

It is well-known [1], however, that the continuum picture is incomplete in the case of brittle fracture in crystalline materials, and one should not omit atomistic effects occurring at the crack tip. We will proceed to present the atomistic framework.

3. Deterministic atomistic setup. In this section, we introduce the atomistic setup by recalling well-established arguments setting out why the continuum picture is insufficient, followed by a detailed discussion on discrete kinematics, Cauchy–Born rule, and atomistic fracture.

3.1. Lattice trapping. Cracks in brittle materials are known to propagate via atomistic mechanisms involving breaking of chemical bonds between atoms at the crack tip [1]. In particular, as first reported in [31] and confirmed for a model similar to ours in [27], the discreteness of the lattice implies that the crack remains locally stable for a range of stress intensity factors

$$(3.1) \qquad I = (K_-, K_+) \subset \mathbb{R},$$

also known as the *lattice trapping range*. This is in contrast with the continuum theory outlined in section 2.3. At the atomistic level, the critical

$$(3.2) \qquad \widetilde{K}_{\text{at}} \in I\bullet$$

corresponds to a unique value for which the atomistic energy is the same both before and after the crack propagating by one lattice spacing ℓ.

3.2. Discrete kinematics. We consider a 2D crystalline material, $\boldsymbol{\Lambda}$, given by the infinite triangular lattice (see Figure 2) defined by

$$(3.3) \qquad \boldsymbol{\Lambda} = \ell\left(\boldsymbol{M}\mathbb{Z}^2 - \widehat{\boldsymbol{x}}\right), \qquad \boldsymbol{M} = \begin{bmatrix} 1 & \frac{1}{2} \\ 0 & \frac{\sqrt{3}}{2} \end{bmatrix}, \qquad \widehat{\boldsymbol{x}} = \begin{bmatrix} \frac{1}{2} \\ \frac{\sqrt{3}}{4} \end{bmatrix},$$

where $\mathbb{Z}^2 = \{(m_1, m_2) \in \mathbb{R}^2 \mid m_1, m_2 \in \mathbb{Z}\}$ and the prefactor $\ell > 0$ is the so-called lattice constant, describing the natural distance between atoms in the material, and
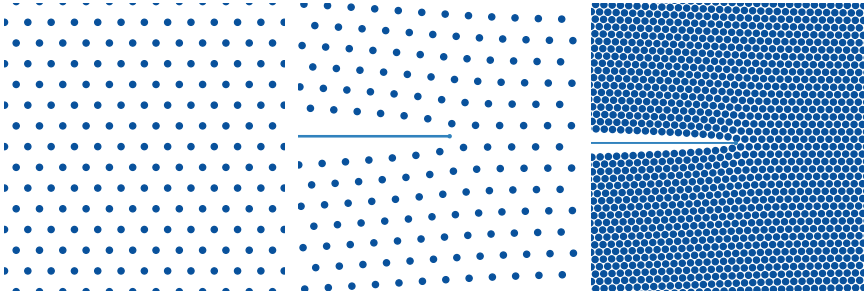

FIG. 2. *Left: A defect-free crystalline material* $\boldsymbol{\Lambda}$. *Middle: The vicinity of a Mode I crack tip with the crack surface depicted as a dotted line. Right: Zoomed-out view of the cracked crystal.*

can be measured experimentally. Conceptually, the 2D domain is to be interpreted as a cross-section of a 3D material body, which is periodic in the antiplane direction. For instance, the triangular lattice is known to be obtained as a projection of the body-centered-cubic lattice [2, Figure 1], which is a crystalline arrangement that can be found in many real-world materials [18].

The atoms are assumed to interact within a finite interaction range $\mathcal{R} \subset \mathbf{\Lambda} \setminus \{\mathbf{0}\}$, which is assumed to respect lattice symmetries, enforced through defining

$$(3.4) \qquad \mathcal{R} = (\mathbf{\Lambda} \setminus \{\mathbf{0}\}) \cap B_{\ell R_*}$$

for some $R_* > 0$, where B_R is the ball of radius R centered at the origin (see Figure 3). The rescaling by the lattice constant ℓ ensures that R_* is an independent parameter, in the sense that R_* uniquely determines the number of atoms in the interaction radius, regardless of the lattice constant.

As noted in section 2.3, we are interested in the in-plane deformations of the material, described by a function $\mathbf{y} : \mathbf{\Lambda} \to \mathbb{R}^2$, and we will use the notation $\mathbf{y}^U$ for

$$\mathbf{y}^U(\mathbf{m}) = \mathbf{m} + \mathbf{U}(\mathbf{m}),$$

where $\mathbf{U} : \Lambda \to \mathbb{R}^2$ is the displacement. For any $\mathbf{m} \in \mathbf{\Lambda}$ and $\boldsymbol{\rho} \in \mathcal{R}$, the finite difference of the deformation at sites $\mathbf{m}$ and $\mathbf{m} + \boldsymbol{\rho}$ is defined as $D_{\boldsymbol{\rho}}\mathbf{y}(\mathbf{m}) = \mathbf{y}(\mathbf{m} + \boldsymbol{\rho}) - \mathbf{y}(\mathbf{m})$. The discrete gradient is then

$$\mathbf{D}\mathbf{y}(\mathbf{m}) := (D_{\boldsymbol{\rho}}\mathbf{y}(\mathbf{m}))_{\boldsymbol{\rho} \in \mathcal{R}} \in \left(\mathbb{R}^2\right)^{\mathcal{R}},$$

where the convenient ordering short-hand notation $\left(\mathbb{R}^2\right)^{\mathcal{R}}$ refers to the space $\mathbb{R}^{2 \times |\mathcal{R}|}$, where $|\mathcal{R}| \in \mathbb{N}$ is the number of elements in $\mathcal{R}$. For the identity deformation $\mathbf{y}^0(\mathbf{m}) = \mathbf{m}$, note that $\mathbf{D}\mathbf{y}^0(\mathbf{m}) = (\boldsymbol{\rho})_{\boldsymbol{\rho} \in \mathcal{R}}$ and so we will sometimes use the notation $(\boldsymbol{\rho})$.

The interaction between atoms is encoded in an interatomic potential $V : \left(\mathbb{R}^2\right)^{\mathcal{R}} \to \mathbb{R}$ with a site energy given by $V(\mathbf{D}\mathbf{y}(\mathbf{m}))$. In the present study, V is restricted to be a pair potential admitting a decomposition of the form
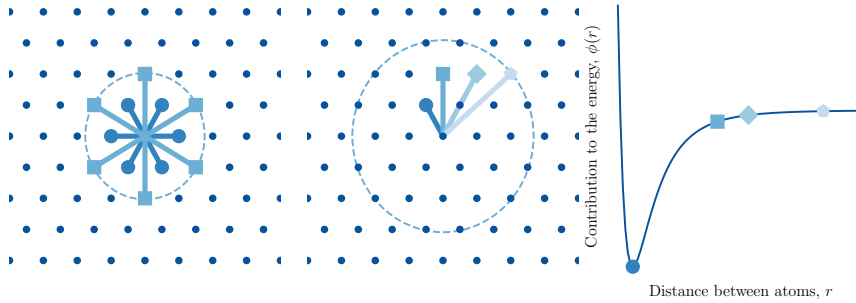
FIG. 3. *Left: The interaction range $\mathcal{R}$ from (3.4) for $R_* = \sqrt{3}$ depicted as a dotted line. All first and second neighbor interaction bonds highlighted. Middle: The interaction range $\mathcal{R}$ from (3.4) for $R_* = \sqrt{7}$ depicted as a dotted line with examples of first, second, third, and fourth neighbors shown. Right: Typical contributions of interaction bonds to the energy for the pair potential ϕ defined in (3.6). Note that when $R_* \geq \sqrt{3}$, it is not typically true for the first neighbor distance to coincide with the minimum of ϕ.*

$$(3.5) \qquad V(\boldsymbol{Dy}(\boldsymbol{m})) = \sum_{\boldsymbol{\rho} \in \mathcal{R}} \phi(|D_{\boldsymbol{\rho}}\boldsymbol{y}(\boldsymbol{m})|),$$

and $\phi : \mathbb{R} \to \mathbb{R}$ is the Lennard–Jones potential [20] given by

$$(3.6) \qquad \phi(r) = 4a_1 \left[\left(\frac{1}{a_2 r} \right)^{12} - \left(\frac{1}{a_2 r} \right)^{6} \right]$$

with two parameters a_1, a_2. Its typical shape is depicted in Figure 3. We note that, usually, the second parameter a_2 is placed in the numerator of the two power terms. As will be discussed in Remark 4.2, in our work, it is more convenient to have it introduced as in (3.6) instead.

The lattice constant ℓ, from (3.3), can be shown to be uniquely determined by a_2 and R_* in our model, that is,

$$(3.7) \qquad \ell(a_2, R_*) = \left(\frac{B_{R_*}}{A_{R_*}} \right)^{1/6} a_2^{-1},$$

where the constants A_{R_*}, B_{R_*} depend on how many neighbors there are in the interaction range. For instance, if we only look at nearest neighbors, i.e., $R_* = 1$, then $A_1 = 1$ and $B_1 = 2$. If $R_* = \sqrt{3}$ (next-to-nearest neighbors also included), then $A_{\sqrt{3}} = 656/27$ and $B_{\sqrt{3}} = 35008/729$. The relevant calculations are outlined in Appendix A.

The resulting energy of the system is formally given by

$$(3.8) \qquad \mathcal{E}(\boldsymbol{U}) = \sum_{\boldsymbol{m} \in \boldsymbol{\Lambda}} V(\boldsymbol{Dy}^{\boldsymbol{U}}(\boldsymbol{m})).$$

3.3. Cauchy–Born rule. As investigated in [9, 11, 7, 25], for example (see also the most recent survey article [8]), a consistent way to link the atomistic model with its continuum counterpart is through the Cauchy–Born rule. In this framework, the interatomic potential, V, the interaction range, $\mathcal{R}$, and the lattice, $\boldsymbol{\Lambda}$, together give rise to a continuum Cauchy–Born strain energy function $W : \mathbb{R}^{2 \times 2} \to \mathbb{R} \cup \{+\infty\}$ through the coupling

$$(3.9) \qquad W(\boldsymbol{F}) := \frac{1}{\det(\ell \boldsymbol{M})} V \left((\boldsymbol{F}\boldsymbol{\rho})_{\boldsymbol{\rho} \in \mathcal{R}} \right),$$

where $\boldsymbol{F} \in \mathbb{R}^{2 \times 2}$ is the displacement gradient arising from the homogeneous displacement field $\boldsymbol{U}(\boldsymbol{x}) = \boldsymbol{F}\boldsymbol{x}$.

A subsequent expansion of W to second order around the identity yields the elasticity tensor $\mathbb{C}$ with

$$(3.10) \qquad \mathbb{C}_{i\alpha j\beta} := \partial_{F_{i\alpha} F_{j\beta}} W(\mathbb{1}) = \frac{1}{\det(\ell \boldsymbol{M})} \sum_{\boldsymbol{\rho}, \boldsymbol{\sigma} \in \mathcal{R}} \partial^2_{i\boldsymbol{\rho} j\boldsymbol{\sigma}} V((\boldsymbol{\rho})) \rho_\alpha \sigma_\beta.$$

In the case of a pair potential, it further simplifies to

$$(3.11) \qquad \mathbb{C}_{i\alpha j\beta} = \frac{1}{\det(\ell \boldsymbol{M})} \sum_{\boldsymbol{\rho} \in \mathcal{R}} \left[\left(\frac{\phi''(|\boldsymbol{\rho}|)}{|\boldsymbol{\rho}|^2} - \frac{\phi'(|\boldsymbol{\rho}|)}{|\boldsymbol{\rho}|^3} \right) \rho_i \rho_j + \delta_{ij} \frac{\phi'(|\boldsymbol{\rho}|)}{|\boldsymbol{\rho}|} \right] \rho_\alpha \rho_\beta.$$

Thus, unlike in the continuum linear elasticity setup, where the elasticities are the independent parameters specifying the material model, here, they are derived quantities and are in effect nonlinear functions of the potential parameters a_1, a_2, introduced

in (3.6), and in principle also of ℓ and R_*. A calculation presented in Appendix A further shows that (2.8) is indeed satisfied and the shear modulus μ is given by

$$(3.12) \qquad \mu = D_{R_*} a_1 a_2^2,$$

where D_{R_*} is a known constant depending on R_*.

3.4. Mode I atomistic fracture. Due to the inherent nonlinearity of the atomistic model, it is not possible to obtain an analytic characterization of atomistic equilibrium configurations around a crack. Away from the crack tip, however, the CLE model outlined in section 2.1, which can be obtained via the Cauchy–Born rule, as discussed in section 3.3, approximates the atomistic model well [3].

The CLE solution $K\widehat{u}$ from (2.9) is thus a suitable far-field boundary condition. We impose this by looking at displacements, $\boldsymbol{U} : \boldsymbol{\Lambda} \to \mathbb{R}^2$, of the form

$$\boldsymbol{U}(\boldsymbol{m}) = K\widehat{\boldsymbol{u}}(\boldsymbol{m} - \boldsymbol{\alpha}) + \boldsymbol{u}(\boldsymbol{m}),$$

where the near-crack-tip *atomistic correction* $\boldsymbol{u}$ is constrained to satisfy

$$(3.13) \qquad |\boldsymbol{Du}(\boldsymbol{m})| \ll |\boldsymbol{D}\widehat{\boldsymbol{u}}(\boldsymbol{m})| \text{ when } |\boldsymbol{m}| \gg 1.$$

This is consistent with the idea presented in the middle panel of Figure 1. The horizontal shift is $\boldsymbol{\alpha} = (\alpha, 0) \in \mathbb{R}^2$, where $\alpha \in \mathbb{R}$ is introduced as a variable to be able to track the crack tip position.

The formally defined infinite lattice energy we wish to equilibrate is given by

$$(3.14) \qquad \mathcal{E}(\boldsymbol{u}, \alpha, K) = \sum_{\boldsymbol{m} \in \boldsymbol{\Lambda}} V(\boldsymbol{Dy}^{\boldsymbol{U}}(\boldsymbol{m})) - V(\boldsymbol{Dy}^{\boldsymbol{0}}(\boldsymbol{m})),$$

where $\boldsymbol{y}^{\boldsymbol{0}}(\boldsymbol{m}) = \boldsymbol{m} + K\widehat{\boldsymbol{u}}(\boldsymbol{m})$. Since in this framework the triplet $(\boldsymbol{u}, \alpha, K)$ fully determines the displacement $\boldsymbol{U}$, we shall often identify $\boldsymbol{U} = (\boldsymbol{u}, \alpha, K)$.

The lattice trapping range I from (3.1) can be found by tracing continuous paths of solutions $(0,1) \ni s \mapsto \boldsymbol{U}_s = (\boldsymbol{u}_s, \alpha_s, K_s)$, such that

$$(\delta_{\boldsymbol{u}} \mathcal{E}(\boldsymbol{U}_s), \delta_\alpha \mathcal{E}(\boldsymbol{U}_s)) = \boldsymbol{0}.$$

As reported in [5] and earlier in [4], the resulting path $s \mapsto \boldsymbol{y}_s$ of equilibrium configurations is expected to be a vertical snaking curve, capturing bond-breaking events, with K_s oscillating within a fixed interval, which is the lattice trapping interval defined in (3.1) (see Figure 4 for an example of a numerically computed snaking curve).

We refer to [3, 4] for a rigorous derivation of the infinite lattice model. As will be noted in section 5, in the present work, we restrict our attention to the case where (3.13) is satisfied through setting $\boldsymbol{u}(\boldsymbol{m}) = \boldsymbol{0} \ \forall \boldsymbol{m} \in \boldsymbol{\Lambda}$, such that $|\boldsymbol{m}| > R_0$ for some suitably chosen R_0.

We further note that the continuum-theory based prediction for the critical stress intensity factor given by (2.10) can be computed for the atomistic model, since the shear modulus μ and the surface energy γ can be computed directly from the atomistic model. It is in fact widely assumed that, in the infinite lattice, the critical stress intensity factor in the atomistic description (3.2) and in the continuum description (2.10) coincide, that is,

$$(3.15) \qquad \widetilde{K}_{\text{at}} = \widetilde{K}_{\text{cont}}.$$

The numerical work presented in section 5 will, among other things, provide evidence that, in our model, this equality holds, subject to accounting for finite-domain effects.
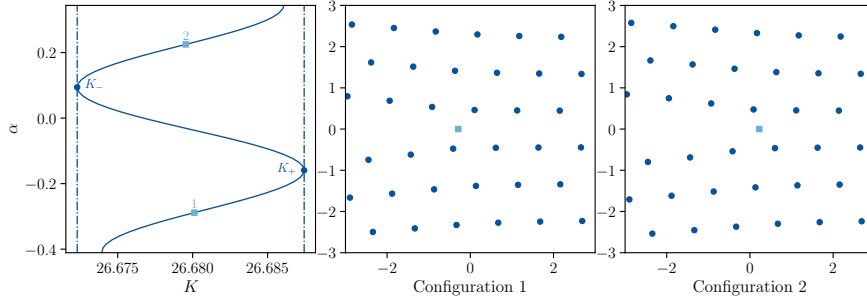
FIG. 4. *Left: The plot $s \mapsto (K_s, \alpha_s)$ showing how K_+ and K_- are identified. The leftward-tilt of the curve is a finite-domain effect—for a theoretical infinite domain the solution curve would be perfectly vertical. Middle and right: atomistic configurations highlighting that a jump by one period on the snaking curve corresponds to the crack propagating by one lattice spacing.*

4. Stochastic atomistic framework.

4.1. An information-theoretic formulation for Lennard–Jones potential. We aim to quantify how the uncertainty in the choice in the model parameters propagates to the computed quantities of interest, which in the case of atomistic fracture are

$$(4.1) \qquad \text{(quantities of interest)} \quad I, \ \widetilde{K}_{\mathrm{at}}, \ \text{and} \ \widetilde{K}_{\mathrm{cont}}.$$

Inspired by the corresponding work in the continuum setup from [13], outlined in section 2.2, we invoke the MaxEnt to infer the probability distributions of parameters present in the model, that is,

$$(a_1, a_2, \ell, R_*) \in \mathbb{R}^4,$$

where we recall that a_1 and a_2 are the potential parameters introduced in (3.6), ℓ is the lattice constant introduced in (3.3), and R_* is the interaction radius from (3.4).

As noted in (3.7), for the Lennard–Jones potential ϕ defined by (3.6), the lattice constant ℓ is uniquely determined by a_2 and R_*, so ℓ is not an independent parameter.

We further recognize the special nature of the interaction radius parameter R_*, which is not a parameter that would typically be considered as a random variable, but rather fixed a priori. Even if it was to be modeled as a random variable, and we note that the information-theoretic stochastic framework provides us with a way of doing so, it would be effectively a countable random variable. For the purpose of analysis, in this section, we consider R_* fixed and later in the numerical section we will consider three deterministic choices for R_*, corresponding to including interaction with up to first, second, and third nearest neighbors, respectively (see Figure 3).

We gather the remaining independent parameters as

$$(4.2) \qquad\qquad\qquad \boldsymbol{A} = (a_1, a_2) \in \mathbb{R}^2.$$

Recalling the set of natural constraints (P1)–(P2) in section 2.2, we first restate (P1) as

$$(4.3) \qquad\qquad\qquad (\mathrm{P1}) \colon \ \mathbb{E}(\boldsymbol{A}) = \underline{\boldsymbol{a}},$$

where $\underline{\boldsymbol{a}} = (\underline{a_1}, \underline{a_2})$ is known, corresponding to default parameters of the potential. The second constraint (P2) concerns the elasticity tensor, which, through the Cauchy–Born rule discussed in section 3.3 and the underlying assumption of planar elasticity

and the pairwise nature of the interatomic potential, simplifies so that the only independent parameter is the shear modulus μ, which, as established in (3.12), is a function of $\boldsymbol{A}$. This leads us to recast (P2) as

$$\text{(4.4)} \qquad \text{(P2): } \mathbb{E}(\log(\mu(\boldsymbol{A}))) = \nu_{\boldsymbol{A}},$$

where $\nu_{\boldsymbol{A}}$ is a given parameter such that $|\nu_{\boldsymbol{A}}| < \infty$. For the rationale as to why the condition of this type ensures (P2) we refer to [13].

PROPOSITION 4.1. *Under the constraints* (4.3) *and* (4.4), *the MaxEnt probability density function of the random variable* $\boldsymbol{A}$ *defined in* (4.2) *is given by*

$$\rho_{\boldsymbol{A}}(\boldsymbol{a}) = \rho_{A_1}(a_1) \times \rho_{A_2}(a_2),$$

where

$$\rho_{A_1}(a_1) = \mathbb{1}_{\mathbb{R}_+}(a_1) k_1 a_1^{-\tau} \exp\{-\lambda_1 a_1\}$$

and

$$\rho_{A_2}(a_2) = \mathbb{1}_{\mathbb{R}_+}(a_2) k_2 a_2^{-2\tau} \exp\{-\lambda_2 a_2\}$$

with k_1 *and* k_2 *positive normalization constants and* λ_1 *and* λ_2 *Lagrange multipliers corresponding to* (P1). *The parameter* τ *controls the level of statistical fluctuations and is required to satisfy* $\tau \in (-\infty, 1/2)$. *It follows that* a_1 *and* a_2 *are statistically independent, with* a_1 *Gamma-distributed with shape and scale hyperparameters* $(\alpha_1, \beta_1) = \left(1 - \tau, \underline{a_1}/(1 - \tau)\right)$ *and* a_2 *Gamma-distributed with shape and scale hyperparameters* $(\alpha_2, \beta_2) = \left(1 - 2\tau, \underline{a_2}/(1 - 2\tau)\right)$.

Proof. The constraints in (4.3) and (4.4), together with the normalization constraint, can be put in the form of a mathematical expectation as in (2.6), namely,

$$\mathbb{E}\{\boldsymbol{g}(\boldsymbol{A})\} = \hat{\boldsymbol{g}},$$

where $\boldsymbol{g} : \mathbb{R}^2 \to \mathbb{R}^4$ with $\boldsymbol{g}(\boldsymbol{A}) = (\boldsymbol{A}, \log(\mu(\boldsymbol{A})), 1) \in \mathbb{R}^4$ and $\hat{\boldsymbol{g}} = (\underline{\boldsymbol{a}}, \nu_{\boldsymbol{A}}, 1) \in \mathbb{R}^4$. It follows from (2.7) that

$$\rho_{\boldsymbol{A}}(\boldsymbol{a}) = \mathbf{1}_{R_+^2}(\boldsymbol{a}) \exp\{-\langle \boldsymbol{\lambda}, \boldsymbol{g}(\boldsymbol{a})\rangle_{\mathbb{R}^4}\},$$

as R_+^2 is the largest set on which (4.4) is satisfied. Since

$$\exp\{-\langle \boldsymbol{\lambda}, \boldsymbol{g}(\boldsymbol{a})\rangle_{\mathbb{R}^4}\} = k_0 \exp(-\lambda_1 a_1) a_1^{-\lambda_3} \exp(-\lambda_2 a_2) a_2^{-2\lambda_3},$$

where $k_0 = \exp(-\lambda_4) D_{R_*}^{-\lambda_3}$, the result follows by identifying $\lambda_3 = \tau$ and an appropriate splitting of the normalization constant as $k_0 = k_1 k_2$. □

Remark 4.2. The Lennard–Jones potential ϕ defined in (3.6) is typically introduced with the second parameter $a_2' := a_2^{-1}$. From the information-theoretic point of view it is far less convenient to do so, as then the MaxEnt distribution of a_2' can be shown (using the framework discussed in this section) to be the Gamma distribution with shape and scale hyperparameters $(1 + 2\tau, a_2'/(1 + 2\tau))$, provided that $\tau \in (-\frac{1}{2}, +\infty)$. Thus, the setup where both a_1 and a_2' follow the Gamma distribution would only apply when $\tau \in (-\frac{1}{2}, 1)$, which is more restrictive than what we obtain in Proposition 4.1.

For the model under consideration, the following can be subsequently established about $\widetilde{K}_{\text{cont}}$.

PROPOSITION 4.3. *The critical stress intensity factor* $\widetilde{K}_{\mathrm{cont}}$, *when computed for the shear modulus* μ *and the surface energy* γ *obtained directly from the atomistic model, satisfies*

$$\widetilde{K}_{\mathrm{cont}} = C_{R_*} a_1 a_2^{3/2},$$

where the constant C_{R_*} *depends only on the interaction range* R_*. *If* $\boldsymbol{A}$ *is taken to follow the MaxEnt distribution established in Proposition* 4.1, *then* $\widetilde{K}_{\mathrm{cont}}$ *is a random variable with the probability density function* $\rho_{\widetilde{K}_{\mathrm{cont}}}$ *given by*

$$\rho_{\widetilde{K}_{\mathrm{cont}}}(k) = \frac{1}{C_{R_*}} \int_{\mathbb{R}} a_2^{-3/2} \rho_{\boldsymbol{A}} \left(\frac{k}{C_{R_*} a_2^{3/2}}, a_2 \right) da_2.$$

Proof. At the atomistic level of description, the energetic cost of creating a surface is equivalent to the energetic cost of breaking interaction bonds between atoms on opposite sides of the surface. We assume first that $R_* = 1$, that is, we only look at the nearest neighbor interaction. In this case, the lattice constant ℓ minimizes the potential ϕ, and in fact $\phi(\ell) = -a_1$. The cost of breaking one bond is then

$$\lim_{r \to \infty} \phi(r) - \phi(\ell) = -\phi(\ell) = a_1.$$

When the crack surface is extended by length L, on the triangular lattice, this corresponds to breaking interaction $2L/\ell$ bonds. Then the surface energy per unit area γ from (2.10) is given by

$$\gamma = \frac{1}{L} \frac{2L}{\ell} \left(\lim_{r \to \infty} \phi(r) - \phi(\ell) \right) = \tilde{C}_1 a_1 a_2,$$

where $\tilde{C}_1 = 2^{5/6}$. This follows from (3.7). It is shown in Appendix A that, in the case of a general R_*, we have

(4.5) $$\gamma = \tilde{C}_{R_*} a_1 a_2.$$

Using (2.10) and (3.12), we then arrive at

$$\widetilde{K}_{\mathrm{cont}} = \frac{4}{\sqrt{3}} \sqrt{\gamma\mu} = C_{R_*} \sqrt{a_1} \sqrt{a_2} \sqrt{a_1} a_2 = C_{R_*} a_1 a_2^{3/2},$$

as required. The probability density function of $\widetilde{K}_{\mathrm{cont}}$ follows from a general formula

$$\rho_{\widetilde{K}_{\mathrm{cont}}}(k) = \int_{\mathbb{R}} \int_{\mathbb{R}} \rho_{\boldsymbol{A}}(\boldsymbol{a}) \delta \left(k - C_{R_*} a_1 a_2^{3/2} \right) da_1 \, da_2,$$

where δ is the Dirac delta. To obtain the result, in the inner integral (in which a_2 is treated as fixed), one performs a change of variables from a_1 to $\tilde{k} = C_{R_*} a_1 a_2^{3/2}$. $\quad\square$

5. Computations. In this section, we employ the stochastic framework developed in section 4.1 to conduct a numerical study of crack propagation.

5.1. Setup. For our numerical computations, we employ the principles of the recently proposed NCFlex scheme [5]. We fix $\tilde{R} = 32$ and consider a computational domain

(5.1) $$\boldsymbol{\Lambda}_R = \boldsymbol{\Lambda} \cap B_R, \quad \text{where} \quad R = \ell(\tilde{R} + 2R_*),$$

then look at displacements $\boldsymbol{U} : \boldsymbol{\Lambda} \to \mathbb{R}^2$ of the form
(5.2)
$$\boldsymbol{U(m)} = K\widehat{\boldsymbol{u}}(\boldsymbol{m}-\boldsymbol{\alpha})+\boldsymbol{u(m)}, \ \ \text{where } \boldsymbol{u(m)} = \boldsymbol{0} \ \forall \boldsymbol{m} \in \boldsymbol{\Lambda} \ \text{such that } |\boldsymbol{m}| > \ell(\tilde{R}+R_*).$$

The rescaling by ℓ ensures that, regardless of the choice of ℓ, for a fixed R_*, the computational domain consists of the same number of atoms $N \sim R^2$. The truncation of $\boldsymbol{u}$ ensures that the finite-dimensional scheme is consistent with (3.13).

We consider three possible choices for R_*, namely,

(i) $R_* = 1$, which corresponds to accounting for only the nearest neighbor interaction;
(ii) $R_* = \sqrt{3}$ (second neighbors included too);
(iii) $R_* = 2$ (up to third neighbors included).

The resulting finite-dimensional approximation to (3.14) is given by

$$\tilde{\mathcal{E}}(\boldsymbol{u}, \alpha, K) = \sum_{m \in \boldsymbol{\Lambda}_R} V(\boldsymbol{Dy}^U(\boldsymbol{m})) - V(\boldsymbol{Dy^0(m)})$$

with $\boldsymbol{y^0}$ as in (3.14).

The essence of the NCFlex scheme is to employ numerical continuation to trace continuous paths of solutions $(0,1) \ni s \mapsto \boldsymbol{U}_s = (\boldsymbol{u}_s, \alpha_s, K_s)$, such that

(5.3)
$$(\delta_{\boldsymbol{u}}\tilde{\mathcal{E}}(\boldsymbol{U}_s), \delta_\alpha\tilde{\mathcal{E}}(\boldsymbol{U}_s)) = \boldsymbol{0}.$$

This is a nonlinear system of $2N + 1$ equations in $2N + 2$ variables, and a numerical continuation constraint closes the system.

The specific numerical algorithm allows for the quantities of interest to be computed without human supervision. The details are presented in Algorithm 1 and we note that the numerical continuation routine is implemented in Julia using `BifurcationKit.jl` [33].

Algorithm 1 Unsupervised NCFlex scheme

1: Given potential parameters a_1, a_2 from (3.6) and some tolerance δ;
2: Estimate the interval $I = (K_-, K_+)$ by fixing $\boldsymbol{u(m)} = 0 \ \forall \boldsymbol{m} \in \boldsymbol{\Lambda}_R$ in (5.2), and solving $\delta_\alpha\tilde{\mathcal{E}}(\boldsymbol{U}) = 0$, up to the tolerance δ, for incremental values of α ranging from $-\ell$ to ℓ (an idea put forward in [5, section II.C.2]);
3: Fix $\alpha = \alpha_0$ (e.g., $\alpha_0 = -0.5$), set $K = K_-$ (estimate found in the previous step), and use a conjugate-gradient solver with initial guess $(\boldsymbol{0}, \alpha_0, K_-)$ to find a static boundary equilibrium $\boldsymbol{U} = (\boldsymbol{u}, \alpha_0, K_-)$ satisfying only $\delta_{\boldsymbol{u}}\tilde{\mathcal{E}}(\boldsymbol{U}) = \boldsymbol{0}$, up to tolerance δ (typically the other equation in (5.3) will not be satisfied);
4: Repeat the previous step for incremental values of $K \in (K_-, K_+)$ (estimate found in step 2) until one identifies K_0 for which $\boldsymbol{U_0} = (\boldsymbol{u_0}, \alpha_0, K_0)$ is such that $\delta_\alpha\tilde{\mathcal{E}}(\boldsymbol{U}) = 0$ (up to tolerance δ) as well, meaning that (5.3) holds true (a bisection-type algorithm can be used to speed up the process);
5: With the first solution $\boldsymbol{U_0}$ of the NCFlex scheme identified, apply the numerical continuation routine outlined in [5, Algorithm 2.] to compute the path of solutions $s \mapsto \boldsymbol{U}_s$.

As noted in section 3.4, the lattice trapping range I and the critical stress intensity factor $\widetilde{K}_{\mathrm{at}}$ can be inferred from the computed solution paths (see Figure 4). Note,

however, that the computed quantities of interest are finite domain approximations. Hence, in particular, $\widetilde{K}_{\mathrm{at}}^R$ computed for a domain with radius R will not match the theoretical $\widetilde{K}_{\mathrm{at}}$ from Proposition 4.3. Therefore, direct comparisons to $\widetilde{K}_{\mathrm{cont}}$ are not feasible. Nevertheless, heuristic considerations and numerical evidence point to the fact that

$$|\widetilde{K}_{\mathrm{at}}^R - \widetilde{K}_{\mathrm{at}}| \sim \mathcal{O}(R^{-1/2}).$$

5.2. Results. We have considered the following cases in our numerical study:

1. $a_1 = 1$ fixed and a sample of 1000 choices of a_2 with $\underline{a_2} = 2^{1/6}$ and $\tau = -20$;
2. $a_2 = 2^{1/6}$ fixed and a sample of 1000 choices of a_1 with $\underline{a_1} = 1$ and $\tau = -20$;
3. a sample of 1000 choices of $\boldsymbol{A}$ with $\underline{a_1} = 1$, $\underline{a_2} = 2^{1/6}$ and $\tau = -20$;
4. a combined sample of 1,000,000 of $\overline{\boldsymbol{A}}$ obtained by reusing the samples from (1) and (2);
5. $a_1 = 1$ fixed, a sample of 1000 choices of a_2 with $\underline{a_2} = 2^{1/6}$ and $\tau = -4{,}000{,}000$ to test the interplay between the strength of statistical fluctuations and the strength of lattice trapping.

Figure 5 presents the level of statistical fluctuations present in ϕ and how this translates to the computed snaking curves. There are several universal conclusions that can be drawn from our numerical investigation, which we shall now discuss and then refer to in the subsequent subsections detailing each case listed above.
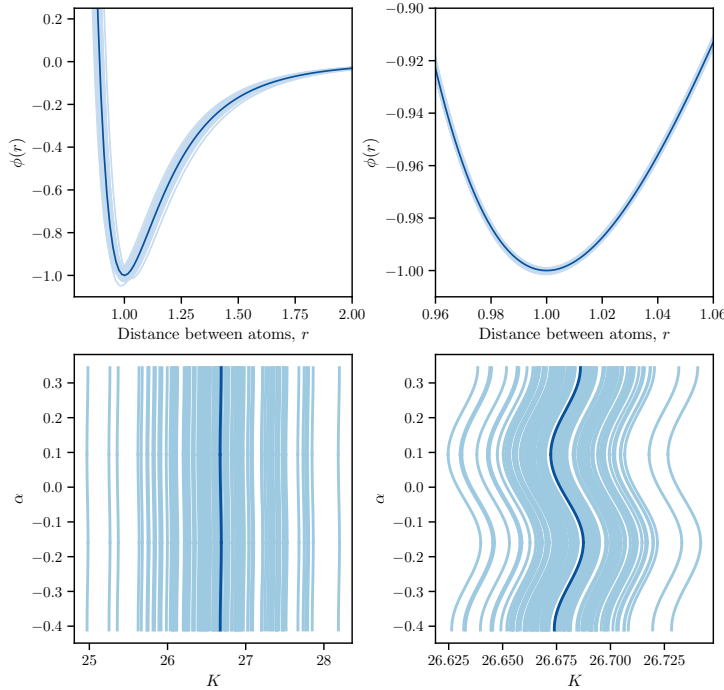

FIG. 5. *Statistical fluctuations for $\tau = -400$ (left column) and $\tau = -4{,}000{,}000$ (right column). Top row: plot of the interatomic potential ϕ for the mean value of parameters (dark blue) and a sample of 100 choices of parameters a_1, a_2 (light blue, on the right zoomed-in around unity to actually see the fluctuations). Bottom row: the resulting computed snaking curves.*

First, it will be numerically verified that the relative strength of the lattice trapping, which we measure as $1 - (K_-/K_+)$, in our model is not a function of a_1 or a_2, but merely of R_*. On a heuristic level, this reflects the fact that the lattice constant ℓ is a linear function of a_2 and is consistent with the work presented in [6]. Our results will also corroborate our conjecture that, in the model considered, K_+ and K_-, for a fixed domain radius R, exhibit the following dependence on a_1, a_2, and R_*,

$$(5.4) \qquad K_+ = C_{R_*}^+ a_1 \, a_2^{3/2}, \quad K_- = C_{R_*}^- a_1 \, a_2^{3/2},$$

differing from $\widetilde{K}_{\text{cont}}$ from Proposition 4.3 only by a constant which depends on R_*. In particular, we will present numerically obtained values for $C_{R_*}^{\pm}$. This is strong evidence that, in fact, the equality $\widetilde{K}_{\text{at}} = \widetilde{K}_{\text{cont}}$ from (3.15) holds true for our model.

Second, the generally nonlinear dependence of quantities of interest on the parameters, as established in Proposition 4.3 and in (5.4), should warrant caution when employing a purely deterministic approach to modeling atomistic fracture. This can be seen, for instance, when comparing $\mathbb{E}(K_+)$ with $K_+(\underline{a_1}, \underline{a_2})$, the relative difference between which will be shown to surpass the strength of the lattice trapping, as inferred also from Table 1. This point is further underlined by looking at the probability of the crack propagating at a given K, to be computed as $\mathsf{P}(K \geq K_+)$, which will be shown to remain nontrivial (i.e., not close to nullity or unity) over a relatively large interval (see Figure 9). It is expected that such issues, which are still manageable in our model, will become even more pronounced for more realistic models (see also the concluding remarks in section 6).

Third, the value of the parameter τ from Proposition 4.1 plays a crucial role in determining whether the extent of lattice trapping is negligible or not. For $\tau = -20$, it most certainly is, and hence, for this case, since $\widetilde{K}_{\text{at}}$ lies somewhere between K_- and K_+, we can safely focus on the outer quantities only. However, as $\tau \to -\infty$, lattice trapping starts to dominate over statistical fluctuations. We show this by considering the extreme case with $\tau = -4{,}000{,}000$.

We now present the results of our numerical study.

Case (1): $a_1 = 1$ fixed, a_2 sampled with $\tau = -20$. We first consider the case where $a_1 = 1$ remains fixed and the parameter a_2 is sampled from the MaxEnt probability distribution established in Proposition 4.1, with $\underline{a_2} = 2^{1/6}$ (corresponding to the lattice constant $\ell = 1$ when $R_* = 1$) and $\tau = -20$. The sample is $\{a_2^{(i)}\}_{i=1}^S$, where $S = 1000$. The probability density function from which the sample was drawn and the histogram of the sample are presented in Figure 6. In this figure, we also present the quantities of interest from (4.1) for $R_* = 1$, $\sqrt{3}$, 2, that is, the probability density function and the histogram of $\{\widetilde{K}_{\text{cont}}^{(i)}\}$ computed via Proposition 4.3, and the histograms of $\{K_{\pm}^{(i)}\}$, with a probability density function fitted according to (5.4).

TABLE 1
Case (1), relevant data as R_* varies: the relative strength of the lattice trapping measured as $1 - K_+/K_-$; the expected value of K_+; the deterministic value of K_+ and constants $C_{R_*}, C_{R_*}^+, C_{R_*}^-$ from Proposition 4.3 and (5.4).

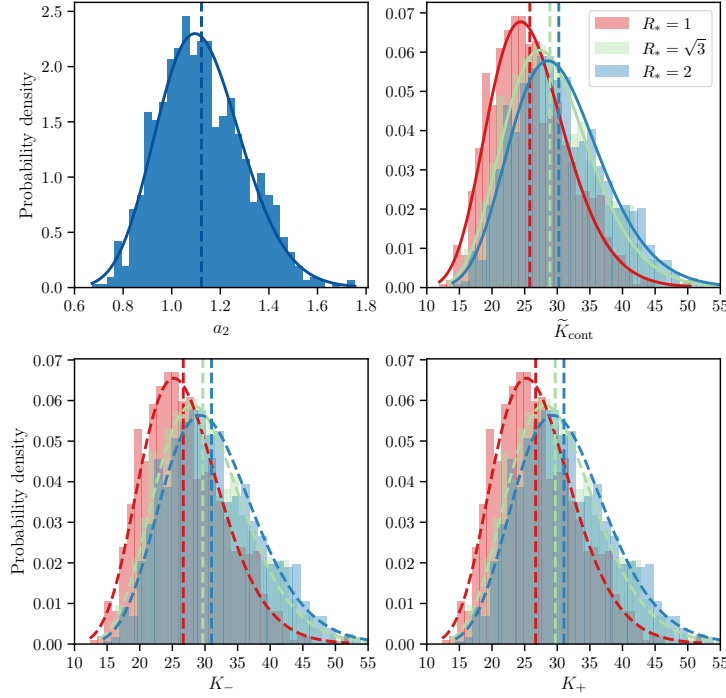| R_*	$1 - K_-/K_+$	$\mathbb{E}(K_+)$	K_+ at $\underline{a_2}$	C_{R_*}	$C_{R_*}^-$	$C_{R_*}^+$
1	0.0005676	26.9643	26.6874	21.6864	22.4286	22.4414
$\sqrt{3}$	0.0006815	29.9944	29.6865	24.2825	24.9462	24.9632
2	0.0007081	31.3467	31.0249	25.4237	26.0702	26.0887

FIG. 6. *Case* (1). *Top left: The normalized histogram of a sample of* 1000 *choices of a_2 drawn from the MaxEnt probability distribution established in Proposition* 4.1, *with $\underline{a_1} = 2^{1/6}$ and $\tau = -20$, together with the probability density function ρ_{A_2}. Top right: The histogram and probability density function for $\widetilde{K}_{\text{cont}}$ from Proposition* 4.3 *for $R_* = 1, \sqrt{3}, 2$. Bottom: The resulting numerically computed histogram of values of K_- (left) and K_+ (right). The dotted lines are numerically predicted probability density functions, based on* (5.4), *with values of $C^+_{R_*}, C^-_{R_*}$ reported in Table* 1. *The dashed vertical lines correspond to the mean value of each sample.*

Table 1 complements the analysis by gathering the relevant data. In particular, we report that the relative strength of the lattice constant only varies with R_* and is rather small, varying from just 0.05% for $R_* = 1$ to 0.07% for $R_* = 2$. The data in Table 1 confirms that $\mathbb{E}(K_+)$ does not equal the deterministic K_+ computed for the mean value of a_2 (the same applies to K_- and $\widetilde{K}_{\text{cont}}$). We also report on the numerically computed values for $C^+_{R_*}$ and $C^-_{R_*}$ from (5.4) and how they compare with C_{R_*}, which can be obtained analytically based on the proof of Proposition 4.3.

Case (2): $a_2 = 2^{1/6}$ fixed, a_1 sampled with $\tau = -20$. Next, we assume that $a_2 = 2^{1/6}$ remains fixed and the parameter a_1 is sampled from the MaxEnt probability distribution established in Proposition 4.1, with $\underline{a_1} = 1$ and $\tau = -20$. The sample is $\{a_1^{(i)}\}_{i=1}^S$, where $S = 1000$. Figure 7 and Table 2 summarize our findings for this case. We note that these results can be obtained very quickly, as the NCFlex scheme only has to be run once due to the following remark.

Remark 5.1. Assume that $\boldsymbol{U} = (\boldsymbol{u}, \alpha, K)$ specifies an equilibrium configuration

$$\boldsymbol{y}^{\boldsymbol{U}}(\boldsymbol{m}) = \boldsymbol{m} + K\widehat{\boldsymbol{u}}(\boldsymbol{m} - \boldsymbol{\alpha}) + \boldsymbol{u}(\boldsymbol{m})$$

that solves (5.3) for some choice of the parameters a_1 and a_2 from the interatomic potential (3.6). It follows from (2.9) that a multiplicative inverse of the shear modulus
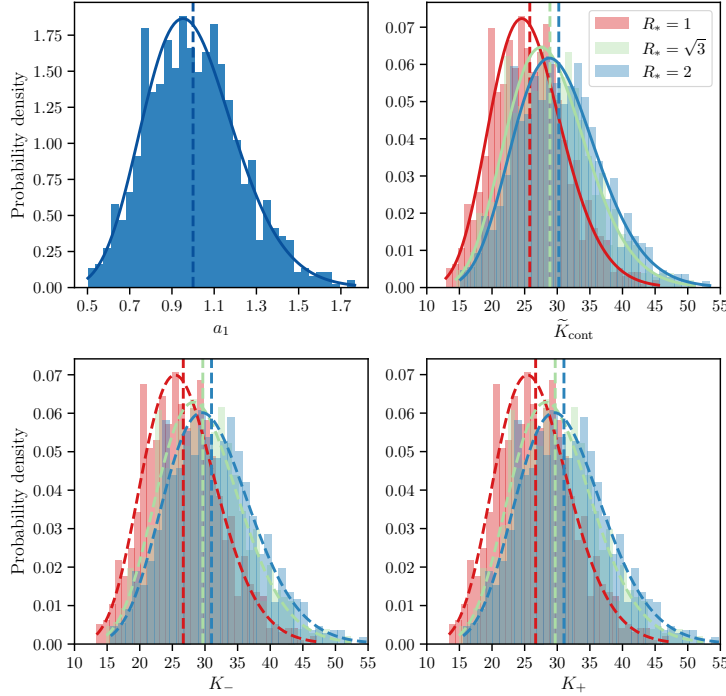
FIG. 7. *Case (2). Top left: the normalized histogram of a sample of* 1000 *choices of* a_1 *drawn from the MaxEnt probability distribution established in Proposition 4.1, with* $\underline{a_1} = 1$ *and* $\tau = -20$, *together with the probability density function* ρ_{A_1}. *Top right: the histogram and probability density function for* $\widetilde{K}_{\mathrm{cont}}$ *from Proposition 4.3 for* $R_* = 1, \sqrt{3}, 2$. *Bottom: the resulting numerically computed histogram of values of* K_- *(left) and* K_+ *(right). The dotted lines are numerically predicted probability density functions, based on (5.4), with values of* $C_{R_*}^+, C_{R_*}^-$ *reported in Table* 2. *The dashed vertical lines correspond to the mean value of each sample.*

TABLE 2
Case (2), relevant data as R_* *varies: the relative strength of the lattice trapping measured as* $1 - K_+/K_-$; *the expected value of* K_+; *the deterministic value of* K_+ *and constants* $C_{R_*}, C_{R_*}^+, C_{R_*}^-$ *from Proposition 4.3 and (5.4). The only differences compared to the data for Case (1) presented in Table* 1 *are highlighted in bold.*

R_*	$1 - K_-/K_+$	$\mathbb{E}(K_+)$	K_+ at $\underline{a_1}$	C_{R_*}	$C_{R_*}^-$	$C_{R_*}^+$
1	0.0005676	**26.8146**	26.6874	21.6864	22.4286	22.4414
$\sqrt{3}$	0.0006815	**29.8280**	29.6865	24.2825	24.9462	24.9632
2	0.0007081	**31.1727**	31.0249	25.4237	26.0702	26.0887

μ enters as a prefactor in $\widehat{\boldsymbol{u}}$, whereas, from (3.12), it follows that the shear modulus μ depends on a_1 linearly. In a pointwise sense, the equilibrium $\boldsymbol{y}^U$ satisfies, for each $\boldsymbol{m} \in \boldsymbol{\Lambda}_R$,

$$\sum_{\boldsymbol{\rho} \in \mathcal{R}} \left[\phi'\big(|D_{\boldsymbol{\rho}} \boldsymbol{y}^U(\boldsymbol{m} - \boldsymbol{\rho})|\big) - \phi'\big(|D_{\boldsymbol{\rho}} \boldsymbol{y}^U(\boldsymbol{m})|\big) \right] = 0,$$

and since a_1 enters as a prefactor in ϕ', it readily follows that

$$(5.5) \qquad \qquad \widetilde{\boldsymbol{U}} = (\boldsymbol{u}, \alpha, K\, a_1/\widetilde{a_1})$$

specifies an equilibrium configuration for the model in which the first parameter in the interatomic potential from (3.6) is set to $\widetilde{a}_1$. As a result, a snaking curve $s \mapsto$

$\boldsymbol{U}_s$ obtained by running the NCFlex scheme for one value of a_1 gives rise to the corresponding snaking curve $s \mapsto \widetilde{\boldsymbol{U}}_s$ via the transformation in (5.5).

This observation implies that working with the 2D random variable $\boldsymbol{A}$ defined in (4.2) is only as computationally costly as working with a_2, so we proceed to Cases (3) and (4).

Case (3): a_1 and a_2 sampled with $\tau = -20$. We now examine the case where both a_1 and a_2 are sampled simultaneously from the MaxEnt probability distribution established in Proposition 4.1, with $\underline{a_1} = 1$, $\underline{a_2} = 2^{1/6}$ (corresponding to the lattice constant $\ell = 1$ when $R_* = 1$) and $\tau = -20$. In particular, the sample is $\{(\tilde{a}_1^{(i)}, \tilde{a}_2^{(i)})\}_{i=1}^S$, where $S = 1000$. We present the resulting data in the form a scatter matrix plot to emphasize the bivariate dependence between the random variables involved. This is shown in Figure 8 for the case when $R_* = 1$. The perfect linear dependence between $\widetilde{K}_{\text{cont}}$ and K_+ provides further numerical evidence that, in fact, (5.4) holds true, rendering the ratio $\widetilde{K}_{\text{cont}}/K_+$ a function of R_* only (for a fixed R). This again strongly hints at the veracity of (3.15). We further see the statistical independence of a_1 and a_2 (by design) and the qualitatively different dependence of the quantities of interest on a_1 and a_2.

Case (4): combining samples of a_1 and a_2 when $\tau = -20$. In this case, we take the samples $\{a_1^{(i)}\}$ from Case (2) and $\{a_2^{(i)}\}$ from Case (1) into a combined 1,000,000 sample $\{(a_1^{(i)}, a_2^{(j)})\}_{i,j=1}^S$, where, as before, $S = 1000$. This is made easy by
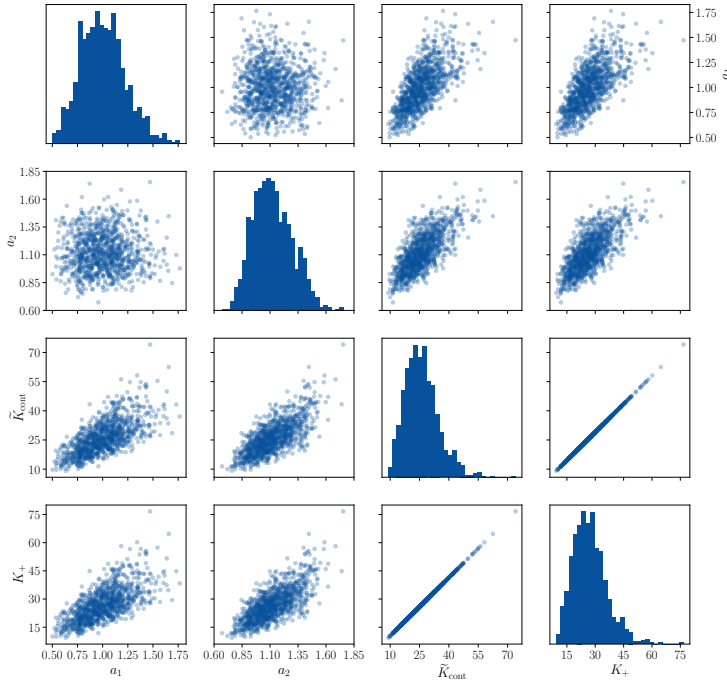

FIG. 8. *Case (3) when $R_* = 1$: a scatter matrix plot for variables a_1, a_2, $\widetilde{K}_{\text{cont}}, K_+$, highlighting bivariate relationships between them (off-diagonal). On the diagonal, histograms of the variables are presented. The plots in particular confirm that K_+ is determined by $\widetilde{K}_{\text{cont}}$ (and the fixed parameters $\tilde{R}$ and R_*). Note that the vertical axis for the plots on the diagonal is different from the ones off-diagonal, hence the placing of the a_1 label in the top-right corner.*

the observation in Case 2, which implies that the NCFlex scheme only has to be run a 1000 times and not a 1,000,000 times. In particular, our focus is on the probability of a crack propagating or not propagating. Due to the phenomenon of lattice trapping, one can distinguish three possibilities:

(4A) if $K < K_-$, then the crack will definitely not propagate;

(4B) if $K_- \leq K < K_+$ (in other words, $K \in I$), then the crack remains lattice-trapped;

(4C) if $K \geq K_+$, then the crack will definitely propagate.

In the lattice-trapped case, thermal fluctuations, typically present at a temperature above absolute zero, imply that there is a nonzero probability of the crack propagating. This is a highly nontrivial case, which we do not delve into, but note that such questions can be approached by combining our approach with the framework of transition state theory [15]. The key quantity here is the energy barrier at different values of K within the lattice trapping range, which can be achieved with the NCFlex scheme. In our stochastic framework, (4A) can be restated as $\mathsf{P}(K < K_-)$, (4B) as $\mathsf{P}(K \in I)$, and (4C) as $\mathsf{P}(K \geq K_+)$. At $\tau = -20$, case (4B) is negligible, hence we omit it from plots and only show (4A) and (4C), both obtained analytically and from the data in Figure 9.

Case (5): as in Case (1), but with $\tau = -4,000,000$. Finally, we revisit the setup from Case (1), but adjust the statistical fluctuations parameter to $\tau = -4,000,000$. In this case, the support of the probability density functions is heavily concentrated around the mean, to the point where the strength of the lattice trapping is comparable with statistical fluctuations. This implies that Case (4B) ceases to be
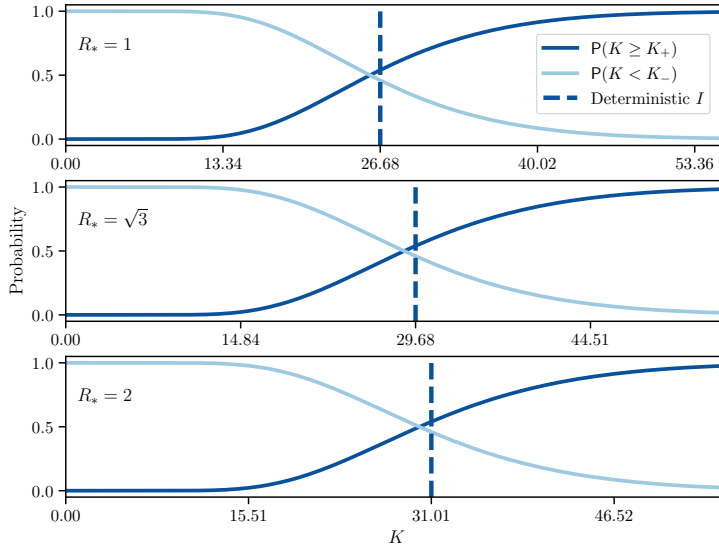

FIG. 9. *Case (4) when $R_* = 1, \sqrt{3}, 2$: the probability of the crack propagating at a given K, computed as $\mathsf{P}(K \geq K_+)$ and of not propagating, computed $\mathsf{P}(K < K_-)$ compared with the deterministic interval $I = (K_-, K_+)$ computed for the mean values $\underline{a_1}$ and $\underline{a_2}$. Note that when $\tau = -20$, the lattice trapping strength is negligible compared to the statistical fluctuations and I can be, effectively, treated as a single value. We further note that the probabilities were computed both analytically (using (5.4) and Proposition 4.3), as well as from data and for a sample of this size they are indistinguishable.*
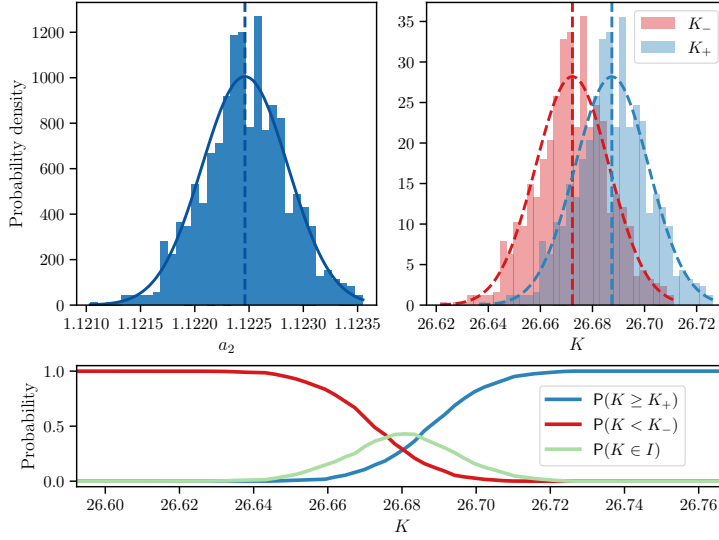
FIG. 10. *Case* (5) *when* $R_* = 1$. *Top left: The normalized histogram of a sample of* 1000 *choices of* a_2 *drawn from the MaxEnt probability distribution established in Proposition* 4.1, *with* $\underline{a_1} = 2^{1/6}$ *and* $\tau = -4,000,000$, *together with the probability density function* ρ_{A_2}. *Top right: The histogram for* K_- *and* K_+, *with the dashed curves representing numerically predicted probability density functions, using* (5.4). *In the top plots, the dashed vertical lines correspond to the mean value of each sample. Bottom: the probability of crack propagation at a given* K, *as in Figure* 9.

negligible. As seen from Figure 10, at this level of statistical fluctuations, there is a significant shift between the probability density functions of K_- and K_+. As a result, for the values of K within the lattice trapping range, $\mathsf{P}(K < K_-)$ and $\mathsf{P}(K \geq K_+)$ are not complementary, in the sense that they do not add up to approximately 1, as can be seen by the considerable probability of $\mathsf{P}(K \in I)$ in-between the mean values of K_- and K_+. Thus the strength of the lattice trapping begins to dominate over the strength of statistical fluctuations. This effect can be more pronounced already at more reasonable values of τ in other models where the lattice trapping range is not as small as in our case.

This concludes our numerical investigation, where we explored an implementation of the stochastic framework introduced in section 4.1.

6. Conclusion. We introduced in this study an information-theoretic stochastic framework for atomistic crack propagation in the analytically tractable case of the so-called theoretical Lennard–Jonesium 2D solid, with the ground state of a triangular lattice and undergoing a pure Mode I fracture. In particular, we invoked the MaxEnt to argue that, when little information is available, except for the mean values of the parameters, the parameters in the Lennard–Jones potential should be modeled as independent, Gamma-distributed random variables. Due to the relative simplicity of the model, we were able to infer how the uncertainty in the choice of these parameters propagates to quantities of interest, which in the case of atomistic fracture is the range of lattice trapping and the value of the critical stress intensity factor. This was followed by an extensive numerical study of stochastic atomistic fracture, made possible by an automated formulation of the NCFlex scheme from [5], which, in particular, highlighted the limitations of a purely deterministic approach.

In future work, we aim to develop a more general information-theoretic approach to uncertainty quantification in atomistic material modeling and further explore the stochastic effects within the lattice trapping range.

The principles of the framework presented in this work are general enough to be applicable to any interatomic potential, including EAM and modern machine-learning potentials. In practice, however, there remain significant, but perhaps manageable, obstacles. In the case of empirical potentials, such as EAM, the key problem is the nonlinear nature of the functional forms, which implies that, unlike in the case of the Lennard–Jones potential, there is no closed form formula for the lattice constant ℓ. In such cases, the equivalent of Proposition 4.1 would establish an intractable joint probability density for the parameters. A promising alternative comes in the form of modern implementations of empirical potentials, which typically use splines to keep functional forms simpler [35]. For instance, one can think of separating neighbors' contributions. In the case of modern machine-learning potentials, the dependence on parameters is typically linear and we hope to exploit the freedom of choice when it comes to defining basis elements, so that the form of the MaxEnt prior distribution of the parameters remains tractable.

Appendix A. Determining the lattice constant, the shear modulus, and the surface energy. In this appendix, we present calculations confirming the veracity of the formulae given by (3.7) and (3.12). Such calculations are well known in the literature but worth elaborating upon since they are central to our stochastic framework. We start with the formally defined energy

$$\mathcal{E}(\boldsymbol{U}) = \sum_{\boldsymbol{m} \in \boldsymbol{\Lambda}_R} V(\boldsymbol{D}\boldsymbol{y}^{\boldsymbol{U}}(\boldsymbol{m})),$$

where $\boldsymbol{\Lambda}_R = \boldsymbol{\Lambda} \cap B_R$. We recall that $\boldsymbol{U}$ is the displacement and $\boldsymbol{y}^{\boldsymbol{U}}(\boldsymbol{m}) = \boldsymbol{m} + \boldsymbol{U}(\boldsymbol{m})$ is the deformation. A formal Taylor expansion of this energy around $\boldsymbol{y^0}$ to second order yields

$$\mathcal{E}(\boldsymbol{y}^{\boldsymbol{U}}) = \mathcal{E}(\boldsymbol{y^0}) + \langle \delta\mathcal{E}(\boldsymbol{y^0}), \boldsymbol{U} \rangle + \langle \delta^2\mathcal{E}(\boldsymbol{y^0})\boldsymbol{U}, \boldsymbol{U} \rangle + \text{h.o.t.},$$

where

$$\langle \delta\mathcal{E}(\boldsymbol{y^0}), \boldsymbol{U} \rangle = \sum_{\boldsymbol{m} \in \boldsymbol{\Lambda}_R} \nabla V((\boldsymbol{\rho})) : \boldsymbol{D}\boldsymbol{U}(\boldsymbol{m}) = \sum_{\boldsymbol{m} \in \boldsymbol{\Lambda}_R} \sum_{i,\boldsymbol{\rho}} \partial_{i\boldsymbol{\rho}} V((\boldsymbol{\rho})) D_{\boldsymbol{\rho}} U_i(\boldsymbol{m})$$

and

$$\langle \delta^2\mathcal{E}(\boldsymbol{y^0})\boldsymbol{U}, \boldsymbol{U} \rangle = \sum_{\boldsymbol{m} \in \boldsymbol{\Lambda}_R} \nabla^2 V((\boldsymbol{\rho})) \boldsymbol{D}\boldsymbol{U}(\boldsymbol{m}) : \boldsymbol{D}\boldsymbol{U}(\boldsymbol{m})$$

$$= \sum_{\boldsymbol{m} \in \boldsymbol{\Lambda}_R} \sum_{i,\boldsymbol{\rho},j,\boldsymbol{\sigma}} \partial^2_{i\boldsymbol{\rho}j\boldsymbol{\sigma}} V((\boldsymbol{\rho})) D_{\boldsymbol{\rho}} U_i(\boldsymbol{m}) D_{\boldsymbol{\sigma}} U_j(\boldsymbol{m}).$$

For a uniform displacement $\boldsymbol{U}$ of the form $\boldsymbol{U}(\boldsymbol{x}) = \boldsymbol{F}\boldsymbol{x}$, for some suitable $\boldsymbol{F} \in \mathbb{R}^{2 \times 2}$, we have $D_{\boldsymbol{\rho}}\boldsymbol{U}(\boldsymbol{x}) = \nabla \boldsymbol{U}(\boldsymbol{x})\boldsymbol{\rho}$. This implies that, for uniform displacements,

(A.1)
$$\langle \delta\mathcal{E}(\boldsymbol{y^0}), \boldsymbol{U} \rangle = \sum_{\boldsymbol{m} \in \boldsymbol{\Lambda}_R} \sum_{i,\alpha=1}^{2} L_{i\alpha} \partial_\alpha U_i,$$

where, due to the form of the potential, we have

$$(A.2) \qquad L_{i\alpha} = \sum_{\boldsymbol{\rho} \in \mathcal{R}} \frac{\phi'(|\boldsymbol{\rho}|)}{|\boldsymbol{\rho}|} \rho_i \rho_\alpha.$$

It is natural to assume that the potential in place admits the perfect lattice as an equilibrium configuration, and for that to be the case, it is necessary that $\langle \delta \mathcal{E}(\boldsymbol{y^0}), \boldsymbol{U} \rangle = \boldsymbol{0}$ for any uniform displacement $\boldsymbol{U}$. It follows that the potential parameters a_1 and a_2 in (3.6) and the lattice constant l have to be chosen so that

$$(A.3) \qquad \sum_{i,\alpha=1}^{2} L_{i\alpha} \partial_\alpha U_i = 0$$

for any $\boldsymbol{U}$. A direct calculation reveals that

$$L_{i\alpha} = 24 a_1 a_2^{-6} \sum_{\boldsymbol{\rho} \in \mathcal{R}} \rho_i \rho_\alpha |\boldsymbol{\rho}|^{-14} \left(|\boldsymbol{\rho}|^6 - 2a_2^{-6} \right).$$

Due to the lattice symmetries in the interaction range $\mathcal{R}$, it is immediate that, for $i, \alpha \in \{1, 2\}$, $L_{i\alpha} = \hat{L} \delta_{i\alpha}$, where δ_{ij} denotes the Kronecker delta and

$$\hat{L} = 24 \frac{a_1 a_2^{-6}}{\ell^{12}} \left(A_{R_*} \ell^6 - B_{R_*} a_2^{-6} \right).$$

The constants depending on R_* are

$$A_{R_*} = \sum_{\hat{\boldsymbol{\rho}} \in \hat{\mathcal{R}}} \hat{\rho}_1^2 |\hat{\boldsymbol{\rho}}|^{-8} \qquad B_{R_*} = \sum_{\hat{\boldsymbol{\rho}} \in \hat{\mathcal{R}}} 2\hat{\rho}_1^2 |\hat{\boldsymbol{\rho}}|^{-14},$$

where $\hat{\mathcal{R}} = \mathcal{R}/\ell$ (i.e., with lattice constant normalized to unity). It follows that the lattice constant ℓ is a function of R_* and a_2, since

$$(A.4) \qquad A_{i\alpha} = 0 \quad \forall i, \alpha \implies \ell = \left(\frac{B_{R_*}}{A_{R_*}} \right)^{1/6} a_2^{-1}.$$

A similar line of reasoning can be used to establish (3.12). The lattice symmetries present in $\mathcal{R}$ imply that the only nonzero entries of the associated elasticity tensor $\mathbb{C}$ from (3.11) are $\mathbb{C}_{iiii}$ $(i = 1, 2)$ and $\mathbb{C}_{iijj} = \mathbb{C}_{ijij}$ $(i = 1, 2$ and $j = 1, 2, j \neq i)$, and, in fact,

$$\mathbb{C}_{iiii} = \frac{1}{\det(\ell \boldsymbol{M})} a_1 \sum_{\hat{\boldsymbol{\rho}} \in \hat{\mathcal{R}}} \hat{\rho}_1^4 \left((B_1 + B_3)|\hat{\boldsymbol{\rho}}|^{-16} - (B_2 + B_4)|\hat{\boldsymbol{\rho}}|^{-10} \right),$$

$$\mathbb{C}_{iijj} = \frac{1}{\det(\ell \boldsymbol{M})} a_1 \sum_{\hat{\boldsymbol{\rho}} \in \hat{\mathcal{R}}} \hat{\rho}_1^2 \hat{\rho}_2^2 \left((B_1 + B_3)|\hat{\boldsymbol{\rho}}|^{-16} - (B_2 + B_4)|\hat{\boldsymbol{\rho}}|^{-10} \right)$$

for known constants $B_1, \ldots, B_4$ depending only on R_*. As a result, we have the shear modulus given by

$$(A.5) \qquad \mu = \frac{1}{3} \mathbb{C}_{1111} = \mathbb{C}_{1122} = \mathbb{C}_{1212} = D_{R_*} a_1 a_2^2,$$

where the dependence on a_2 enters through (A.4). Finally, we also show the surface energy computation that confirms (4.5). Let d_n denote the distance to the nth neighbor in the triangular lattice, with lattice constant equal to unity, and let N_* be the unique value such that $d_{N_*} \leq R_*$, but $d_{N_*+1} > R_*$. For example, if $R_* = 2$, then $N_* = 3$, since $d_1 = 1$, $d_2 = \sqrt{3}$, and $d_3 = 2$. If the crack surface is extended by L, then $m_n L/\ell$ bonds of length d_n additionally cross from one side of the crack to another. For example, $m_1 = 2$ (two nearest-neighbor bonds cross the surface in the triangular lattice if we extend the surface by one lattice spacing) and $m_2 = 4$. Importantly, m_n is a fixed constant for each n. The energetic cost of breaking each such bond is given by $-\phi(d_n\ell)$. In the light of the above, a general formula for the surface energy γ can be stated as

$$\gamma = \frac{1}{L}\frac{L}{\ell}\left(\sum_{n=1}^{N_*} -m_n\phi(d_n\ell)\right).$$

For a general R_*, the relationship between ℓ and a_2 established in (3.7) implies that, for any scalar α, we have

$$\phi(\alpha\ell) = 4a_1 a_2^{-6}\alpha^{-6}\frac{A_{R_*}}{B_{R_*}}a_2^6\left(a_2^{-6}\alpha^{-6}\frac{A_{R_*}}{B_{R_*}}a_2^6 - 1\right) =: Ca_1,$$

where the constant C depends only on α and R_*, as the terms involving a_2 cancel each other. Putting it all together, by gathering all the different constants depending only on R_* we conclude that

$$\gamma = \tilde{C}_{R_*}a_1 a_2,$$

where the constant $\tilde{C}_{R_*}$ only depends on R_*.

REFERENCES

[1] E. BITZEK, J. R. KERMODE, AND P. GUMBSCH, *Atomistic aspects of fracture*, Int. J. Fracture, 191 (2015), pp. 13–30.

[2] J. BRAUN, M. BUZE, AND C. ORTNER, *The effect of crystal symmetries on the locality of screw dislocation cores*, SIAM J. Math. Anal., 51 (2019), pp. 1108–1136.

[3] M. BUZE, T. HUDSON, AND C. ORTNER, *Analysis of an atomistic model for anti-plane fracture*, Math. Models Methods Appl. Sci., 29 (2019), pp. 2469–2521.

[4] M. BUZE, T. HUDSON, AND C. ORTNER, *Analysis of cell size effects in atomistic crack propagation*, ESAIM Math. Model. Numer. Anal., 54 (2020), pp. 1821–1847.

[5] M. BUZE AND J. R. KERMODE, *Numerical-continuation-enhanced flexible boundary condition scheme applied to mode-*i *and mode-*iii *fracture*, Phys. Rev. E, 103 (2021), 033002.

[6] W. A. CURTIN, *On lattice trapping of cracks*, J. Mater. Res., 5 (1990), pp. 1549–1560.

[7] W. E AND P. MING, *Cauchy-Born rule and the stability of crystalline solids: Static problems*, Arch. Ration. Mech. Anal., 183 (2007), pp. 241–297.

[8] J. L. ERICKSEN, *On the Cauchy-Born rule*, Math. Mech. Solids, 13 (2008), pp. 199–220.

[9] J. L. ERICKSEN, *The Cauchy and Born hypotheses for crystals*, in Phase Transformations and Material Instabilities in Solids, M. E. Gurtin, ed., 1984, pp. 61–77.

[10] S. L. FREDERIKSEN, K. W. JACOBSEN, K. S. BROWN, AND J. P. SETHNA, *Bayesian ensemble approach to error estimation of interatomic potentials*, Phys. Rev. Lett., 93 (2004), 165501.

[11] G. FRIESECKE AND F. THEIL, *Validity and failure of the Cauchy-Born hypothesis in a two-dimensional mass-spring lattice*, J. Nonlinear Sci., 12 (2002), pp. 445–478.

[12] J. GUILLEMINOT, *Modeling non-Gaussian random fields of material properties in multiscale mechanics of materials*, in Uncertainty Quantification in Multiscale Materials Modeling, Y. Wang and D. L. McDowell, eds., Elsevier Ser. Mech. Adv. Mat., Woodhead Publishing, Sawston, UK, 2020, pp. 385–420.

[13] J. GUILLEMINOT AND C. SOIZE, *On the statistical dependence for the components of random elasticity tensors exhibiting material symmetry properties*, J. Elasticity, 111 (2013), pp. 109–130.

[14] J. Guilleminot and C. Soize, *Non-Gaussian random fields in multiscale mechanics of heterogeneous materials*, Encyclopedia Contin. Mech., H. Altenbach and A. Öchsner, eds., Springer, Berlin, 2020, pp. 1826–1834.

[15] P. Hänggi, P. Talkner, and M. Borkovec, *Reaction-rate theory: Fifty years after Kramers*, Rev. Modern. Phys., 62 (1990), pp. 251–341.

[16] E. T. Jaynes, *Information theory and statistical mechanics*, Phys. Rev., 106 (1957), pp. 620–630.

[17] J. R. Kermode, T. Albaret, D. Sherman, N. Bernstein, P. Gumbsch, M. C. Payne, G. Csányi, and A. De Vita, *Low-speed fracture instabilities in a brittle crystal*, Nature, 455 (2008), pp. 1224–1227.

[18] C. Kittel, P. McEuen, and P. McEuen, *Introduction to Solid State Physics*, 8th ed., Wiley, New York, 1996.

[19] L. D. Landau, E. M. Lifshitz, and J. B. Sykes, *Theory of Elasticity*, Course Theoret. Phys., Pergamon Press, Oxford, 1989.

[20] J. E. Lennard-Jones, *On the determination of molecular fields.* III. *From crystal measurements and kinetic theory data*, Proc. A, 106 (1924), pp. 709–718.

[21] S. Longbottom and P. Brommer, *Uncertainty quantification for classical effective potentials: An extension to potfit*, Model. Simul. Mater. Sci. Eng., 27 (2019), 044001.

[22] M. M. Mehrabadi and S. C. Cowin, *Eigentensors of linear anisotropic elastic materials*, Quart. J. Mech. Appl. Math., 43 (1990), pp. 15–41, doi: 10.1093/qjmam/43.1.15.

[23] M. L. Mehta, *Random Matrices*, Elsevier, New York, 2004.

[24] L. A. Mihai, T. E. Woolley, and A. Goriely, *Stochastic isotropic hyperelastic materials: Constitutive calibration and model selection*, Proc. A, 474 (2018), 20170858, doi: 10.1098/rspa.2017.0858.

[25] C. Ortner and F. Theil, *Justification of the Cauchy-Born approximation of elastodynamics*, Arch. Ration. Mech. Anal., 207 (2013), pp. 1025–1073.

[26] M. Ostoja-Starzewski, *Lattice models in micromechanics*, Appl. Mech. Rev., 55 (2002), pp. 35–60.

[27] J. E. Sinclair, *The influence of the interatomic force law and of kinks on the propagation of brittle cracks*, Philos. Mag., 31 (1975), pp. 647–671.

[28] C. Soize, *Non-Gaussian positive-definite matrix-valued random fields for elliptic stochastic partial differential operators*, Comput. Methods Appl. Mech. Engrg., 195 (2006), pp. 26–64.

[29] C. Soize, *Uncertainty Quantification: An Accelerated Course with Advanced Applications in Computational Engineering*, Inter. Disp. Appl. Springer, Berlin, 2017.

[30] C. T. Sun and Z.-H. Jin, *Fracture Mechanics*, Academic Press, New York, 2012.

[31] R. Thomson, C. Hsieh, and V. Rana, *Lattice trapping of fracture cracks*, J. Appl. Phys., 42 (1971), pp. 3154–3160.

[32] M. F. Thorpe and I. Jasiuk, *New results in the theory of elasticity for two-dimensional composites*, Proc. Math. Phys. Sci., 438 (1992), pp. 531–544.

[33] R. Veltz, *BifurcationKit.jl*, https://hal.archives-ouvertes.fr/hal-02902346, 2020.

[34] M. Wen and E. B. Tadmor, *Uncertainty quantification in molecular simulations with dropout neural network potentials*, npj Comput. Mater., 6 (2020), pp. 1–10.

[35] M. Wen, S. M. Whalen, R. S. Elliott, and E. B. Tadmor, *Interpolation effects in tabulated interatomic potentials*, Model. Simul. Mater. Sci. Eng., 23 (2015), 074008.

[36] A. T. Zehnder, *Fracture Mechanics*, Springer, Berlin, 2012.